Phys Chem Minerals (2006) 33: 347–355
DOI 10.1007/s00269-006-0081-2

ORIGINAL PAPER

Sylvie Demouchy · Stephen Mackwell

# Mechanisms of hydrogen incorporation and diffusion in iron-bearing olivine

Received: 20 September 2005 / Accepted: 27 February 2006 / Published online: 11 April 2006


**Abstract** The incorporation and diffusion of hydrogen in San Carlos olivine ($Fo_{90}$) single crystals were studied by performing experiments under hydrothermal conditions. The experiments were carried out either at 1.5 GPa, 1,000°C for 1.5 h in a piston cylinder apparatus or at 0.2 GPa, 900°C for 1 or 20 h in a cold-seal vessel. The oxygen fugacity was buffered using Ni–NiO, and the silica activity was buffered by adding San Carlos orthopyroxene powders. Polarized Fourier transform infrared (FTIR) spectroscopy was utilized to quantify the hydroxyl distributions in the samples after the experiments. The resulting infrared spectra reproduce the features of FTIR spectra that are observed in olivine from common mantle peridotite xenoliths. The hydrogen concentration at the edges of the hydrogenated olivine crystals corresponds to concentration levels calculated from published water solubility laws. Hydrogen diffusivities were determined for the three crystallographic axes from profiles of water content as a function of position. The chemical diffusion coefficients are comparable to those previously reported for natural iron-bearing olivine. At high temperature, hydrogenation is dominated by coupled diffusion of protons and octahedrally coordinated metal vacancies $\left(V''_{Me}\right)$, where the vacancy diffusion rate limits the process. From the experimental data, we determined the following diffusion laws (diffusivity in $m^2\ s^{-1}$, activation energies in kJ $mol^{-1}$): $D_{V_{Me}[100],[010]} = 10^{-4.5\pm4.1} \exp[-(204 \pm 94)/RT]$ for diffusion along [100] and [010]; $D_{V_{Me}[001]} = 10^{-1.4\pm0.5} \exp[-(258 \pm 11)/RT]$ for diffusion along [001]. These diffusion rates are fast enough to modify significantly water contents within olivine grains in xenoliths ascending from the mantle.

**Keywords** Olivine · Hydrogen · Point defects · Diffusion · Polarized FTIR spectroscopy

S. Demouchy · S. Mackwell
Bayerisches Geoinstitut, Universität Bayreuth, 95440 Bayreuth, Germany

S. Mackwell
Lunar and Planetary Institute, 3600 Bay Area Blvd, Houston , TX 77058, USA

*Present address*: S. Demouchy (✉)
Department of Geology and Geophysics, University of Minnesota, 310 Pillsbury Drive SE, Minneapolis, MN 55455, USA
E-mail: demou005@umn.edu

## Introduction

Water embedded as hydrogen in the structure of the nominally anhydrous minerals (NAMs) olivine, garnet and pyroxene (Miller et al. 1987; Bell and Rossman 1992; Kohlstedt et al. 1996; Ingrin and Skogby 2000) has a substantial effect, even at very low concentration levels, on many physical and chemical characteristics of the rock comprising Earth's upper mantle. A small amount of water lowers the viscosity of mantle minerals and rocks (e.g., Chopra and Paterson 1984; Mackwell et al. 1985; Karato et al. 1986; Mei and Kohlstedt 2000), reduces the melting temperature in the upper mantle (e.g., Gaetani and Grove 1998), modifies phase equilibria and petrologic processes (e.g., Arndt et al. 1998; Muentener et al. 2001), and increases electrical conductivity (e.g., Karato 1990; Wanamaker 1994; Constable and Duba 2002; Hirth et al. 2000). It has also been proposed that the presence of water (hydrogen) in mantle rocks might be a critical factor for the initiation of plate tectonics (Regenauer-Lieb et al. 2001; Regenauer-Lieb and Kohl 2003).

Despite the agreement within the scientific community on the importance of water in mantle rocks at the microscopic, macroscopic and geological scales, the incorporation mechanisms and the mobility of hydrogen at the atomistic level in olivine are still topics of debate. Laboratory experiments are critical for providing the thermodynamic and kinetic data necessary to predict and to understand water capacity (i.e., 'water solubility') and transport (i.e., 'diffusivity') in the deep Earth. However, based on Fourier transform infrared (FTIR) spectroscopy, it has recently been argued that laboratory

experiments designed to study the incorporation of hydrogen into olivine poorly reproduce the infrared spectra from mantle-derived olivine (Matveev et al. 2001, 2004; Berry et al. 2005). These authors suggest that experimental results on hydrogen diffusion are therefore of questionable merit.

The present study aims (1) to show that hydration experiments do in fact reproduce the FTIR characteristics of equilibrated olivine grains from mantle rocks, and (2) to constrain more fully the speciation and transport rate of the hydrogen in olivine. Hydration experiments were performed on crystals of San Carlos olivine to provide a direct comparison with previous studies (Mackwell and Kohlstedt 1990; Bai and Kohlstedt 1992; Kohlstedt et al. 1996; Kohlstedt and Mackwell 1998).

## Starting material and experimental methods

We used olivine crystals from San Carlos (Arizona, USA) that have no cracks or optically visible inclusions. The chemical composition of this starting material, $Mg_{0.904}Fe_{0.092}Ni_{0.0035}Cr_{0.0003}SiO_4$, was measured using a Cameca SX50 electron microprobe (15 eV, 15 nA point beam and 20 s counting time, average over 20 points). The samples were cut with faces perpendicular to each crystallographic axis (±5°) and polished using diamond films from 30 to 0.5 μm. The final sample sizes were 2.99×1.81×1.52 $mm^3$ (SC-33A), 1.39×1.84×3.00 $mm^3$ (SC-33B), and 2.5×2.6×2.3 $mm^3$ (SC-32A and SC-33B), measured parallel to [100], [010] and [001], respectively. The olivine crystals were pre-equilibrated by annealing at 1,300°C for 20 h at room pressure at an oxygen fugacity of $10^{-7.3}$ atm (i.e., near the Ni–NiO buffer) controlled by a CO–$CO_2$ gas mixture. This step is necessary in order to dry the samples and to equilibrate the point defect concentrations in the crystals to levels near those during the subsequent hydrothermal anneals. Subsequently, FTIR analyses were performed to verify the dry state of the sample prior to the hydrothermal annealing experiment.

Hydrogenation experiments (Table 1) were performed either in a piston-cylinder (PC) apparatus or in titanium–zirconium–molybdenum (TZM) cold-seal vessels:

1. The PC experiments were performed at a pressure of 1.5 GPa ± 0.1% (with a friction correction of 20%, and pressure calibration from Bromiley and Keppler 2004) and a temperature of 1,000°C for 5 h (±3 s). Calibrated Talc-Pyrex™ cells (Hudson et al. 1994) were used with an alumina cylinder and plugs around the capsule and a tapered graphite furnace. The temperature was controlled using a $Pt_{100\%}$–$Pt_{90\%}Rh_{10\%}$ thermocouple (i.e., type S—no corrections were made for the effect of pressure on the measured temperature). The temperature gradient along the sample capsule is estimated to be less than

**Table 1** Experimental conditions of hydration for olivine samples, hydrogen concentration of annealed olivine and chemical diffusion coefficients along each axis

| Sample | App | Temperature (°C) | *P* (GPa) | Time (±0.01, h) | log $fO_2^a$ | Capsule | wt ppm $H_2O^b$ (H/$10^6$ Si) | $\tilde{D}$ [100] ($m^2$ $s^{-1}$) | $\tilde{D}$ [010] ($m^2$ $s^{-1}$) | $\tilde{D}$ [001] ($m^2$ $s^{-1}$) |
|---|---|---|---|---|---|---|---|---|---|---|
| SC 32-G | PC | 1,000 | 1.5 | 5 | −10.3 | $Pt_{0.95}$–$Rh_{0.05}$ | 13 ± 1[c] (212 ± 16) | ND | (3 ± 1)×$10^{-13}$ | ND |
| SC 32-B | PC | 1,000 | 1.5 | 5 | −10.3 | $Pt_{0.95}$–$Rh_{0.05}$ | 16 ± 2[c] (261 ± 33) | ND | (3 ± 1)×$10^{-13}$ | ND |
| SC 33-A | TZM | 900 | 0.2 | 20 | −11.9 | Pt | 20 ± 2 (327 ± 33) | (5 ± 5)×$10^{-13}$ | (5 ± 2)×$10^{-14}$ | (1 ± 0.5)×$10^{-12}$ |
| SC 33-B | TZM | 900 | 0.2 | 1 | −11.9 | Pt | 10 ± 1 (163 ± 16) | (4 ± 0.5)×$10^{-11}$ | (2 ± 1)×$10^{-12}$ | (1 ± 1)×$10^{-12}$ |

Hydrogen concentrations were obtained using the calibration of Bell et al. (2003)

*App* high pressure and high temperature apparatus, *PC* piston cylinder, *TZM* titanium–zirconium–molybdenum cold-seal vessel, *ND* not determined because of the poor quality of the sample, it was not possible to take a profile parallel to this direction

[a] log $fO_2$ calculated according to O'Neill and Wall (1987) for the Ni–NiO buffer

[b] Hydrogen concentration at the rim of the sample (for the three crystallographic directions)

[c] Because of the poor quality of the sample, it was not possible to perform an infrared analysis with *E*//[001], so measurements were made with *E*//[100] only. Therefore, the maximum amount of hydrogen reported here is less than the solubility

25°C for the conditions applied (Bromiley and Keppler 2004). We released the pressure over 3 days. However, even with such a caution, the single crystals were cracked, presumably during depressurization. We welded the samples inside $Pt_{0.95}$–$Rh_{0.05}$ capsules along with 10 µl of liquid water (neither brucite nor talc were used).
2. The TZM cold-seal experiments were performed at a pressure of 0.2 GPa and temperature of 900°C for experimental durations of 1 or 20 h. The capsules in these experiments were pure platinum, and we included 20 µl of liquid water.

For both sets of experiments, olivine crystals were packed in a mixture of San Carlos olivine powder with San Carlos orthopyroxene powder at a ratio of 10:1 in order to buffer the activity of silica. Both olivine and orthopyroxene crystals used to prepare the packing powder were hand picked and selected from the same San Carlos xenolith. Ni-foil and NiO powder (for the PC experiments) or mixed Ni–NiO powders (for the TZM experiments) were added to control the oxygen fugacity during the experiments (Table 1). The oxygen fugacity, $fO_2$, for each experiment was calculated using the data from O'Neill and Wall (1987). After each experiment, the recovered capsule was pierced with a needle to check for excess water (fluid or gas) to ensure that the system was water saturated. All experiments reported here showed excess water after the experiment, so that the fluid pressure during the experiment was equal to the confining pressure. We also verified, using optical microscopy, that neither component of the buffer (Ni and NiO) had been totally consumed, giving confidence that the oxygen and water fugacities are well constrained.

## Transmission electron microscope

Transmission electron microscope (TEM) observations were performed using a FEG TEM (200 kV) at the Bayerisches Geoinstitut on sample SC33-B after the experiment to check whether these samples contained water-rich precipitates, hydrous defect layers (e.g., humite lamellae, Miller et al. 1987), high dislocation densities, or melt pockets (e.g., the early partial melting phenomenon of Raterron et al. 2000). Selected area diffraction and observations in high resolution TEM were carried out in the hydrated regions as well as in the anhydrous part of the sample.

## Fourier transform infrared spectroscopy

The hydroxyl distributions within our samples were analyzed using polarized FTIR spectroscopy collected with a Bruker™ IFS 120 HR high-resolution FTIR spectrometer coupled with a Bruker™ IR microscope. The technical setup is identical to that described by Demouchy and Mackwell (2003). The FTIR spectrometer contains all-reflecting Cassegranian optics and is equipped with a metal-strip polarizer on a KRS-5 substrate. Analyses in the microscope were made at room temperature and pressure, under a stream of $H_2O$- and $CO_2$-free purified air. Near-infrared (NIR) measurements were performed using a tungsten light source, a $Si/CaF_2$ beam splitter and high-sensitivity narrow-band MCT (mercury–cadmium–telluride) detector cooled by liquid nitrogen. Two hundred scans were accumulated for each spectrum at a resolution of 1 $cm^{-1}$. The infrared beam was focused in the middle of the sample using a 1.5 mm aperture, which generates a spot size of 100 µm in the focal plane. Due to the divergence of the infrared beam, the associated spot size on the surface of a 1 mm sample is around 600 µm. In order to increase spatial resolution parallel to the diffusion direction, especially close to sample edges, we used an aluminum mask fixed to the objective lens of the microscope to reduce the angle of incidence from 30° to 10°, yielding a spot size at the sample surface of around 270 µm parallel to the direction of diffusion.

First, we characterized each sample by taking spectra with the electric vector ($E$) parallel to each axis and with the beam focused close to the edges. Second, we took a series of IR spectra (profiles) parallel to the [100], [010] and [001] crystallographic axes with $E$ parallel to [001]. Spectra were collected at a spacing of 30–50 µm near the edges and 100–300 µm near the center of the sample. After background-baseline correction and thickness normalization to 1 cm, the hydroxyl content, $C_{OH}$, was determined for each spectrum using the relationship

$$C_{OH} = \frac{1}{I}\int k(v)\,dv \tag{1}$$

with

$$I = I_{//}\gamma, \tag{2}$$

where $k(v)$ is the absorption coefficient at wave number $v$, $I//$, the integral extinction coefficient (here taken to be 5.32 $cm^{-2}$ per wt ppm $H_2O$, according to Bell et al. 2003), and, $\gamma$ is the orientation factor (equal to 1 in the case of polarized spectra with the polarization direction parallel to the O–H bond direction, Paterson 1982; Bell et al. 2003). Integration was performed between 3,650 and 3,100 $cm^{-1}$. The solubility of hydroxyl in iron-bearing olivine is the sum of the concentrations determined using Eq. 1 for infrared measurements with $E$ parallel to the three orthogonal crystal axes.

## Diffusion analysis

The diffusivity of hydrogen in olivine can be determined from the plots of water content versus distance across the samples, as in previous studies on olivine and forsterite (Mackwell and Kohlstedt 1990; Kohlstedt and Mackwell 1998, 1999; Demouchy and Mackwell 2003).

The data were fit using a solution to Fick's second law for diffusion from an infinite source into a finite slab for a short time (Carslaw and Jaeger 1959); for a profile in one dimension

$$C_{\mathrm{OH}}(x) = C_0\left(\mathrm{erfc}\frac{x}{2\sqrt{\tilde{D}_i t}} + \mathrm{erfc}\frac{X-x}{2\sqrt{\tilde{D}_i t}}\right), \quad (3)$$

where $C_{\mathrm{OH}}$ $(x)$ is the hydroxyl concentration at a distance $x$ from the first sample edge, $X$, the width of the sample, $t$, the time, erfc, the complementary error function, $C_0$, the maximum water content for the given infrared beam polarization (with $E$ parallel to [001] in this study), and, $\tilde{D}_i$, the chemical diffusivity for the mobile species parallel to $i$=[100], [010] or [001] under the experimental conditions. When profiles were taken along a particular direction, measurements were made along a line in the middle of the sample, in order to minimize overlapping between profiles from the different directions. However, in order to estimate potential overlapping of the profiles and to validate the one-dimension approach, three-dimensional diffusion profiles were calculated. The diffusion in three-dimensions can then be described by the function $v(x,y,z)$ (Carslaw and Jaeger 1959), where the width of the grain in the $x$ direction is $2a$, in the $y$ direction $2b$ and in the $z$ direction $2c$:

$$\begin{aligned} v(x,y,z) = {} & \frac{64}{\pi^3}\sum_{l=0}^{\infty}\sum_{m=0}^{\infty}\sum_{n=0}^{\infty}\frac{(-1)^{l+m+n}}{(2l+1)(2m+1)(2n+1)} \\ & \times \cos\frac{(2l+1)\pi x}{2a}\cos\frac{(2m+1)\pi y}{2b}\cos\frac{(2n+1)\pi z}{2c} \\ & \times \left[\exp -\frac{\pi^2 t}{4}\left\{\frac{D_x(2l+1)^2}{a^2} + \frac{D_y(2m+1)^2}{b^2} \right.\right. \\ & \left.\left. + \frac{D_z(2n+1)^2}{c^2}\right\}\right] + C_{\mathrm{i}}. \end{aligned} \quad (4)$$

Here $v$ $(x, y, z)$ is the water concentration at point $(x, y, z)$, $t$, the time, $C_{\mathrm{i}}$, the initial hydroxyl content, $D_{(\mathrm{x,\ y,\ z})}$, the chemical diffusivity for the mobile species parallel to [100], [010] and [001], respectively. For the SC 33-B and SC 33-B crystals, with $2a$ = 2.45 mm, $2b$ = 2.6 mm and $2c$ = 2.3mm, we used $D_x = 5\times10^{-13}$ m$^2$ s$^{-1}$, $D_y = 5\times10^{-14}$ m$^2$ s$^{-1}$ and $D_z = 1\times10^{-12}$ m$^2$ s$^{-1}$ at 900°C, based on the one-dimensional analysis for hydrogen diffusion in iron-bearing olivine limited by metal vacancy diffusion (Table 1). In their previous studies, Mackwell and Kohlstedt (1990) and Kohlstedt and Mackwell (1998) identified two distinct mechanisms of H incorporation based on point defect thermodynamics and observed differences in anisotropy of diffusion. Here, we report briefly the characteristics of the two mechanisms and establish unambiguously the identity of the diffusing species: (1) In experiments at low temperatures ( ≤ 900°C) for short experimental durations (~1 h at 900°C), hydrogen incorporation occurs by exchange of protons with polarons, electron holes localized on iron atoms occupying octahedrally coordinated metal cation sites (Mackwell and Kohlstedt 1990; Kohlstedt and Mackwell 1998, 1999). As the maximum polaron content of olivine under anhydrous conditions (i.e., nominally the ferric iron concentration) is on the order of 100 atomic ppm at low pressures (Nakamura and Schmalzried 1983; Tsai and Dieckmann 1997, 2002), this "redox-exchange" process only permits the incorporation of a limited amount of hydrogen. This process is rate limited by proton diffusion and yields proton self-diffusivities of $\sim10^{-10}$m$^2$s$^{-1}$ at 1,000°C; proton diffusion is also strongly anisotropic with the fastest direction of diffusion parallel to [100] (Mackwell and Kohlstedt 1990). According to Kohlstedt and Mackwell (1998), the chemical diffusivity (i.e., the diffusion rate obtained from the measured diffusion profiles), $\tilde{D}_{\mathrm{exch}}$, for the incorporation of hydrogen by redox exchange is given by

$$\tilde{D}_{\mathrm{exch}} = \frac{2D_{\mathrm{p}}D_{\mathrm{H}}}{D_{\mathrm{p}} + D_{\mathrm{H}}}, \quad (5)$$

where $D_{\mathrm{p}}$ is the polaron diffusivity, and $D_{\mathrm{H}}$ is the proton self-diffusivity. Since

$$\begin{aligned} & D_{\mathrm{p}} \gg D_{\mathrm{H}}, \\ & \tilde{D}_{\mathrm{exch}} \approx 2D_{\mathrm{H}}. \end{aligned} \quad (6)$$

At higher temperatures (≥900°C) and/or longer experimental durations ( > 3 h at 900°C), additional hydrogen is incorporated by a second process, here referred to as the "proton-vacancy" process, that involves defect associates formed between protons and intrinsic point defects, argued to be metal vacancies by Kohlstedt and Mackwell (1998, 1999). In this case, the olivine sample can incorporate more hydrogen, with up to 135 wt ppm $H_2O$ (2,200 H/10$^6$ Si) at 2.5 GPa and 1,100°C (Kohlstedt et al. 1996, using the calibration of Paterson 1982). More recently and using the improved calibration by Bell et al. (2003), Mosenfelder et al. (2006) reported higher hydrogen concentration around ~2,000 wt ppm $H_2O$ at ~6 GPa and 1,000°C. The incorporation of hydrogen by this coupled proton-vacancy process occurs at $\sim10^{-12}$ m$^2$ s$^{-1}$ in olivine at 1,000°C, with the fastest diffusion parallel to [001]. The chemical diffusivity for the incorporation of hydrogen linked to metal vacancies is given by Kohlstedt and Mackwell (1998):

$$\tilde{D} = \frac{3D_{V_{\mathrm{Me}}}D_{\mathrm{H}}}{2D_{V_{\mathrm{Me}}} + D_{\mathrm{H}}}, \quad (7)$$

where $\tilde{D}$ is the chemical diffusivity determined from the experiments, $D_{V_{\mathrm{Me}}}$, the diffusivity of metal vacancies and $D_{\mathrm{H}}$ is the self-diffusivity of protons. As, generally, $D_{\mathrm{H}} \gg D_{V_{\mathrm{Me}}}$ (Kohlstedt and Mackwell 1998)

$$\tilde{D} \approx 3D_{V_{\mathrm{Me}}}. \quad (8)$$

Given the modest amount of hydrogen that can be diffused by the redox-exchange process, this proton-

vacancy process is expected to be the dominant and limiting mechanism of H transport in olivine under upper mantle conditions.

## Results

### Infrared spectra and hydrogen concentration

Polarized FTIR spectra from hydrated olivine samples after a short-anneal experiment (SC 33-B, 900°C, 0.2 GPa, 1 h) and after a long-anneal experiment (SC 33-A, 900°C, 0.2 GPa, 20 h) are compared in Fig. 1 with spectra of olivine from a garnet-bearing peridotite xenolith embedded in alkali basalt from Pali-Aike, Chile

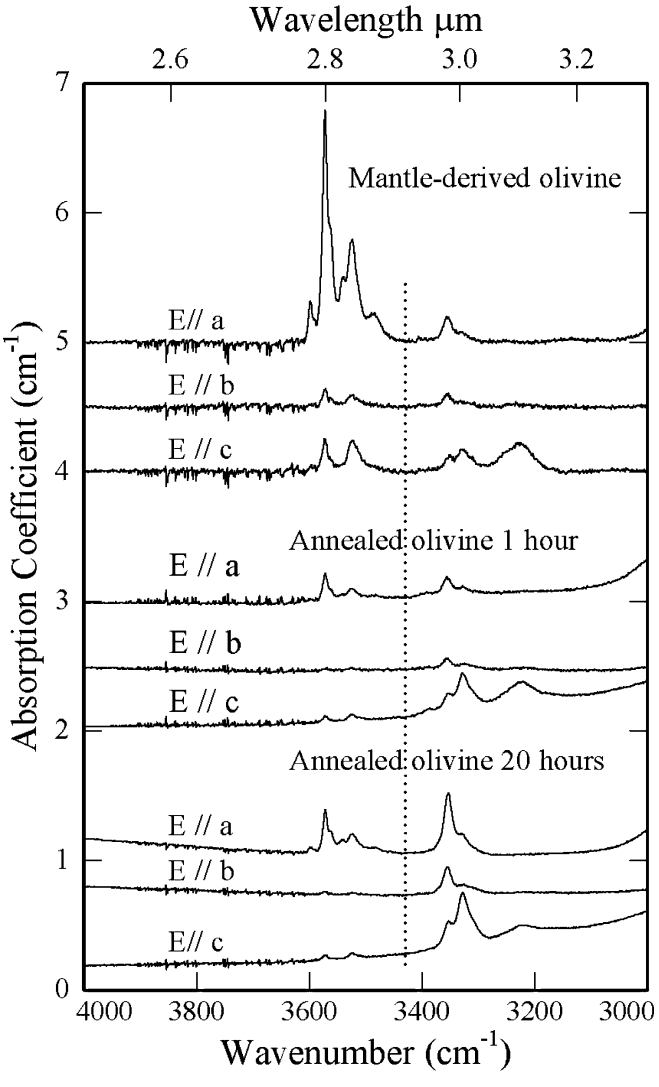


**Fig. 1** Polarized IR spectra, with different orientations of *E*, for olivine samples SC 33-A (after an experiment at 900°C, 0.2 GPa, 20 h duration, buffered by Ni–NiO) and SC 33-B (after an experiment at 900°C, 0.2 GPa, 1 h duration and buffered by Ni–NiO). Polarized IR spectra, with different orientations of *E*, for mantle-derived olivine from Pali-Aike, Chile, also given for comparison (Demouchy et al. 2006)

(Demouchy et al. 2006). Two groups of infrared bands are distinguishable: (1) group I, at high wave number, from 3,616 to 3,450 $cm^{-1}$, and (2) group II, at lower wave number, from 3,450 to 3,200 $cm^{-1}$. With *E* parallel to [100], group I is the dominant group with respect to band intensity. With *E* parallel to [010], both groups are reduced in intensity, indicating that the group I bands result from O–H bonds mostly subparallel to [100]. With *E* parallel to [001], group II is the principal group with respect to band intensity. Band positions were not observed to change with experimental duration. The maximum hydrogen concentration observed in the olivine samples are given in Table 1, which was calculated from polarized infrared spectra for *E* parallel to the three orthogonal directions using the calibration of Bell et al. (2003), varies from $10 \pm 1$ wt ppm $H_2O$ ($163 \pm 16$ H/$10^6$ Si, sample SC 33-B) to $20 \pm 2$ wt ppm $H_2O$ ($327 \pm 33$ H/$10^6$ Si, sample SC 33-A). Our results are comparable to those from previous hydration experiments on olivine (Mackwell and Kohlstedt 1990; Kohlstedt and Mackwell 1999; Bai and Kohlstedt 1992) in which the calibration from Paterson (1982) was used (i.e., if the correction factor of 3.5, recommended by Bell et al. (2003), is applied).

The absence of IR bands related to lamellae of hydrous minerals (e.g., amphibole, serpentine, and clinohumite), is consistent with the TEM observations of the hydrated regions near the sample edges as well as of the anhydrous interior that revealed no precipitates, linear or planar defects.

### Diffusion rates and anisotropy

The chemical diffusivities determined from the infrared profiles in olivine samples parallel to each axis are given in Table 1. Samples recovered from the PC experiments were too damaged to measure infrared profiles along all crystallographic axes; only diffusion parallel to [010] was investigated. In Fig. 2, one series of polarized infrared spectra are plotted as absorption coefficient versus wave number and position in sample SC 33-A with *E*//[001] and diffusion parallel to [001]. The intensity of the hydroxyl infrared bands is the highest at the edges and decreases toward the middle of the sample until a minimum absorption coefficient corresponding to ~4 wt ppm $H_2O$ (65 H/$10^6$ Si) is reached. The corresponding diffusion profiles for each axis are plotted in Fig. 3 for samples SC 32-G, SC 32-B, SC33-A and SC33-B with *E* parallel to [001]. The best fits of the data to the diffusion law in Eq. 3 yield the chemical diffusivities in Fig. 3. The fits were performed under the assumption that all hydroxyl bands vary as a function of position in the same way as for those with *E* parallel to [001]. While some data deviate somewhat from the fitted curves, most fall within the uncertainty limits of the FTIR measurements. These deviations often resulted from small imperfections at the surface or small conchoidal fractures on the sample edges. In Fig. 4, the self-diffusivities for H and

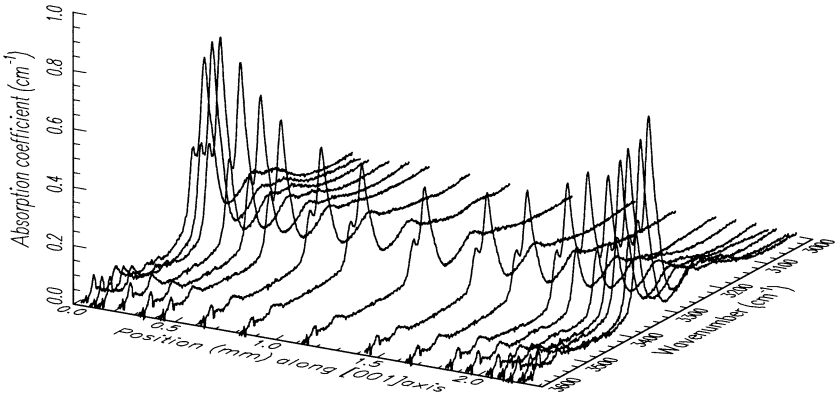


**Fig. 2** Series of polarized infrared spectra with $E//[001]$ as a function of position parallel to [001] in sample SC 33-A after an experiment at 0.2 GPa, 900°C, for 20 h buffered with Ni–NiO

metal vacancies are plotted as a function of temperature for diffusion parallel to each of the olivine crystal axes.

## Discussion

### Infrared band position and $a_{SiO_2}$

In theory, each infrared band corresponds to a distinct type of hydrous point defect. However assigning infrared bands to a given point defect is a current topic of debate. Recently, Matveev et al. (2001) suggested, on the basis of measurements of experimentally hydrated olivine, that the two groups of IR bands result from differences in silica activity. Their olivine samples, from a xenolith collected at Mont Pordon, Australia, were annealed under hydrous conditions in the presence of periclase or orthopyroxene powder to impose different silica activities. Oxygen fugacity was either controlled by a Re–ReO buffer, which is 1.2–1.4 log units more oxidizing than that set by fayalite–magnetite–quartz (Matveev et al. 2001), or not explicitly controlled using a calibrated oxygen buffer (Matveev et al. 2004). They report the following: (1) If olivine co-exists with magnesiowüstite (i.e., low silica activity), the group I IR bands (high wave number) are well developed, and the group II IR bands (low wave number) are almost absent. Matveev et al. (2001) conclude that group I IR bands are due to OH linked to vacant tetrahedral cation (silicon) sites. (2) If olivine co-exists with orthopyroxene (high silica activity), the group II IR bands are well developed and group I bands are very weak. Matveev et al. (2001) suggest that the group II bands arise from OH linked to vacant octahedral cation (metal) sites. These observations were again reported in Matveev et al. (2004). Olivines from mantle xenoliths (Miller et al. 1987; Bell et al. 2003; Matsyuk and Langer 2004) show in most cases IR bands in both groups. Consequently, Matveev et al. (2001, 2004) suggest that a metasomatic fluid/melt overprints a low silica activity (involving the presence of periclase) onto the initial high silica activity imposed by the presence of orthopyroxene. Furthermore, Matveev et al. (2004) suggest that it is possible to estimate the silica activity of magmas from the IR hydroxyl features in its co-existing olivine phenocrysts.

From our data (Fig. 1) and previous experimental studies (Mackwell and Kohlstedt 1990; Bai and Kohlstedt 1992, 1993; Zhao et al. 2004), it is clear that, in contradiction to the claims of Matveev et al. (2001, 2004), experimentally hydrated olivine buffered using orthopyroxene does show IR features including both group I and group II bands. Furthermore, the shape and the positions of the IR bands are in excellent agreement with mantle-derived olivine (Fig. 1). While the IR band positions are the same, the intensities of the bands vary between the laboratory annealed and naturally occurring olivines. Thus, the use of Ni–NiO to buffer the $fO_2$ and orthopyroxene to buffer $a_{SiO_2}$, as already pointed out by Bai and Kohlstedt (1992, 1993), reproduces well the IR hydroxyl features in mantle olivine. We suggest that the relative intensities of the two groups can only be adequately explained by the differences in thermochemical environment (e.g., $fO_2$, temperature, iron content, $a_{SiO_2}$) between the various experimental studies, and not simply by the differences in $a_{SiO_2}$. Although our experiments were performed along the Ni–NiO buffer, near the expected oxidation state of the uppermost mantle (Mattioli and Wood 1986; McCammon 2005), we would expect some variation in the concentration of a given population of defects due to differences in the other relevant thermochemical parameters. Thus, the unambiguous assignment of individual infrared bands to specific defects in olivine is clearly not yet established.

The presence of titanium has also been suggested to be necessary to reproduce the IR features observed from natural olivine grains and explain the differences between experimentally hydrated olivine and mantle-derived olivine (Berry et al 2005). In their study, Berry et al. (2005) attributed the IR bands near ~3,572 and 3,525 $cm^{-1}$, regularly observed in natural olivine, to the presence of Ti-clinohumite-like defects (TEM investigations have not been reported to confirm the presence of such defects in the samples studied by Berry et al. 2005). In addition, experimental study on hydrated forsterite indicates that Ti- and Fe-free forsterite samples show weak infrared bands at 3,527 $cm^{-1}$ (Demouchy and

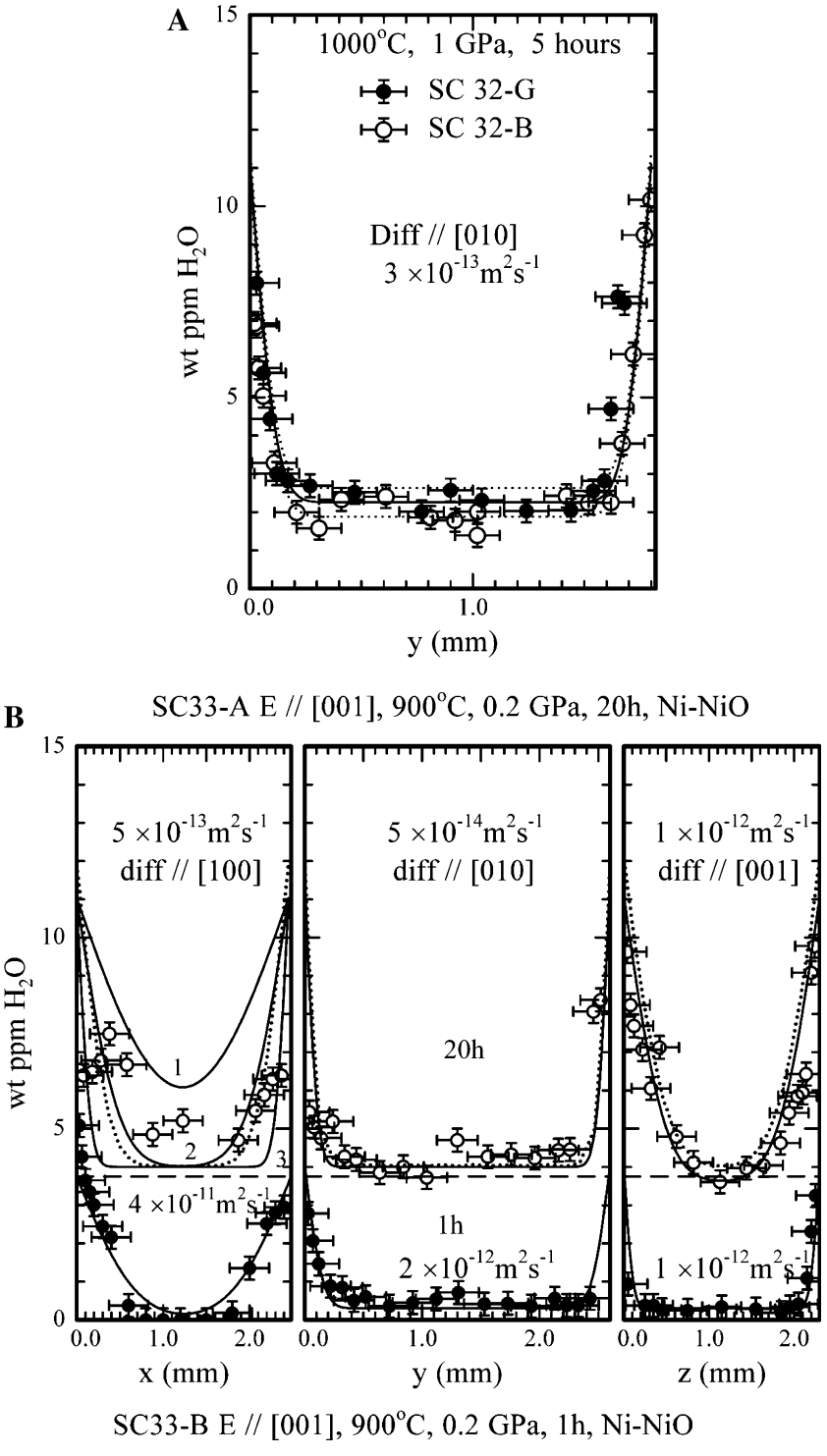


**Fig. 3** **a** Hydroxyl content as a function of position parallel to the crystallographic axis ($y$ = [010]) for samples SC 32-G and SC 32-B after a hydrogenation experiment at 1.5 GPa, 1,000°C, 5 h, buffered with Ni–NiO. The *solid curve* represents the solution to the diffusion law (Eq. 3), the *dotted curves* give other possibilities for the same diffusion coefficient for a hydrogen concentration ±0.4 wt ppm $H_2O$ in the central part of the profile. **b** Hydroxyl content as a function of position parallel to each crystallographic axis ($x$ = [100], $y$ = [010], $z$ = [001]) for sample SC 33-A after a hydrogenation experiment at 0.2 GPa, 900°C, 20 h, buffered with Ni–NiO, and sample SC 33-B after a hydrogenation experiment at 0.2 GPa, 900°C, 1 h, buffered with Ni–NiO. The *solid curves* represent the solution to the diffusion law (Eq. 3). Additional calculations are presented in the this plot: *solid curve* (*1*) initial concentration = 4 wt ppm $H_2O$ and $D_x = 1\times10^{-12}$ m$^2$ s$^{-1}$, *solid curve* (*2*) initial concentration = 4 wt ppm $H_2O$ and $D_x = 5\times10^{-12}$ m$^2$ s$^{-1}$, *solid curve* (*3*) the initial concentration = 4 wt ppm $H_2O$ and $D_x = 1\times10^{-13}$ m$^2$ s$^{-1}$, the *dotted curves* are the results of the three-dimensional model using the one-dimensional diffusivities from Table 1. These curves are consistent with the one-dimensional approach, indicating no significant issues with overlapping of the profiles. The chemical diffusion coefficient, $\tilde{D}$, is given for each axis. Errors in the diffusion coefficients are given in Table 1

Mackwell 2003) and 3,577 cm$^{-1}$ (Lemaire et al. 2003; see also Zhao et al. 2004).

## Mechanisms of hydrogen diffusion

The point defect self-diffusivities ($D_H$ and $D_{V_{Me}}$) obtained from the chemical diffusivities ($\tilde{D}_{exch}$ and $\tilde{D}$) from this study and that of Kohlstedt and Mackwell (1998) were fit using a least squares regression to the following Arrhenius relation:

$$\tilde{D}_i = \tilde{D}_i^0 \exp(-Q_i/RT). \quad (9)$$

Taking into account the factor of 2 from Eq. 6, the hydrogen self-diffusion coefficient for the incorporation by redox-exchange along [100] is $(2\pm0.5)\times10^{-11}$ m$^2$ s$^{-1}$

at 900°C, which is slightly slower than results from previous studies of $5\times10^{-11}$ $m^2$ $s^{-1}$ at 900°C (Mackwell and Kohlstedt 1990). An absorption coefficient corresponding to ~4 wt ppm $H_2O$ (65 H/$10^6$ Si) is reached at the sample surface by this process. This background corresponds to hydrogen incorporated by the redox-exchange process mostly before substantial diffusion by the proton-vacancy process.

The diffusivities reported here (Table 1 and Fig. 4) for the proton-vacancy mechanism of hydrogen incorporation were combined with previous results (Kohlstedt and Mackwell 1998) in order to determine the activation energy for diffusion. Therefore, taking into account that the second mechanism of hydrogen diffusion is limited by the metal-vacancy self-diffusivity (Eq. 8), hydrogen incorporation can be described for the three crystallographic axes by the following relationships (diffusivity given in $m^2$ $s^{-1}$ and activation energies given in kJ $mol^{-1}$):

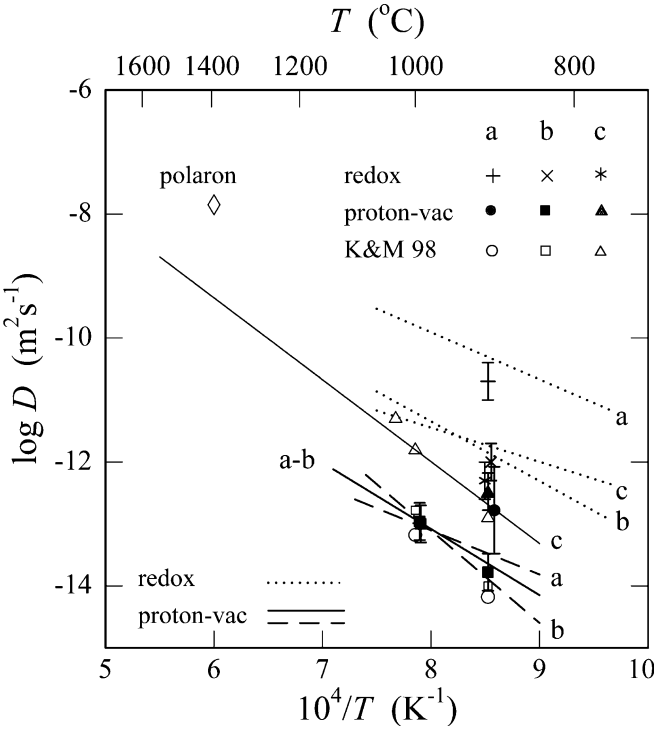


**Fig. 4** Self-diffusivities for metal vacancies and hydrogen ions in olivine. The linear (*cross*, *plus* and *asterisk*) and *filled symbols* are the results from this study. The *open symbols* are the previous results from Kohlstedt and Mackwell (1998) for the proton-vacancy process. Data from this study were fitted with the data from Kohlstedt and Mackwell (1998) to obtain better diffusion laws. The *solid line a–b* is the best fit for the proton-vacancy process in olivine parallel to [100] and [010]. The *dotted lines* represent the results from Kohlstedt and Mackwell (1998) for hydrogen diffusion by redox exchange. The *solid line c* for the [001] direction represents a linear fit to the compilation of data for metal vacancy diffusion in iron-bearing olivine from this study and previous publications (Nakamura and Schmalzried 1983, 1984; Mackwell et al. 1988; Kohlstedt and Mackwell 1998). The *diamond symbol* represents the polaron diffusivity calculated by Sato (1986) from electrical conductivity measurements

$$D_{V_{Me}[100],[010]} = 10^{-(4.5\pm4.1)}\exp[-(204\pm94)/RT],$$

$$D_{V_{Me}[001]} = 10^{-(1.4\pm0.5)}\exp[-(258\pm11)/RT].$$

Although the chemical diffusivities for the two mechanisms are the same for diffusion parallel to [001], the self-diffusivity for vacancies is slower than that for hydrogen ions and yields a higher activation energy (258 vs. 110 kJ $mol^{-1}$). This second mechanism allows substantially more incorporation of water-derived species into the olivine, and likely generates hydroxyl concentrations that are in equilibrium with the thermochemical environment.

## Application to Earth's interior

From the diffusion law for hydrogen in olivine given in this study, it is clear that a loss or gain of water by redox-exchange and coupled proton-vacancy mechanisms will occur in times that are very short relative to the geological timescale. Thus, modification of the original mantle water content in xenolithic olivine is expected to occur as they are brought to Earth's surface, although a complete reequilibration of an olivine grain to the new (water-saturated or undersaturated) environment during ascent is unlikely. Consequently, the water content in xenolithic olivine crystals is at best only a partial reflection of the water content of the source region in the upper mantle. These predictions from experimental studies were recently confirmed by the observation of hydrogen diffusion profiles (dehydration) in olivine from a mantle xenolith in alkali basalt from Pali-Aike, Chile (Demouchy et al. 2006). This study demonstrated that "natural" profiles of hydrogen diffusion, combined with experimental diffusion results can be used to provide constraints on the kinetics of ascent for xenoliths and magma toward Earth's surface.

## Conclusions

(1) The present study demonstrates that laboratory hydration experiments are able to reproduce features in FTIR spectra of mantle-derived olivine. (2) The study confirms two distinct mechanisms of hydrogen incorporation in olivine. (3) For the proton-vacancy process of hydrogen incorporation rate limited by metal vacancy self-diffusion, diffusion along the [100] and [010] axes is significantly slower than along the [001] axis. (4) These diffusion rates are fast enough to modify significantly water contents of olivine grains in xenoliths ascending from the mantle.

**Acknowledgements** The authors thank F. Langenhost for the TEM observations. S.D. thanks D.L Kohlstedt for valuable comments, D. Frost and A. Berry for animated discussions in Vienna. The authors would like also to acknowledge J. Mosenfelder and an anonymous reviewer for their thorough reviews, which have significantly improved the manuscript. This work was supported by

the European Community though the Human Potential Programme HPRN-CT-2000-00056, HydroSpec (to S.D.) and by the NSF EAR-0337012 (to S.J.M.). This paper is LPI publication #1284.

## References


Arndt NT, Ginibre C, Chauvel C, Albarède F, Cheadle M, Herzberg C, Jenner G, Lahaye Y (1998) Were Komatiites wet? Geology 26:739–742

Bai Q, Kohlstedt DL (1992) Substantial hydrogen solubility in olivine and implications for water storage in the mantle. Nature 357:672–674

Bai Q, Kohlstedt DL (1993) Effects of chemical environment on the solubility and incorporation mechanism for hydrogen in olivine. Phys Chem Miner 19:460–471

Bell D, Rossman G (1992), Water in Earth's mantle: the role of nominally anhydrous minerals. Science 255:1391–1397

Bell DR, Rossman GR, Maldener J, Endisch D and Rauch F (2003) Hydroxide in olivine: a quantitative determination of the absolute amount and calibration of the IR spectrum. J Geophys Res 108:B2 , ECV 8–1/9, doi: 1029/2001JB000679

Berry A, Hermann J, O'Neill HSC, Foran GJ (2005) Fingerprinting the water site in mantle olivine. Geology 33:869–872

Bromiley GD, Keppler H (2004) An experimental investigation of hydroxyl solubility in jadeite and Na-rich clinopyroxenes. Contrib Mineral Petrol 147(2):189–200

Carslaw HS, Jaeger JC (1959) Conduction of head in solids, 2nd edn. Clarendon, Oxford, p 510

Chopra PN, Paterson MS (1984) The role of water in the deformation of dunite. J Geophys Res 89:7861–7876

Constable S, Duba A (2002) Diffusion and mobility of electrically conducting defects in olivine. Phys Chem Miner 29:446–454

Demouchy S, Mackwell SJ (2003) Water diffusion in synthetic iron-free forsterite. Phys Chem Miner 30:486–494

Demouchy S, Jacobsen SD, Gaillard F, Stern CR (2006) Rapid magma ascent recorded by water diffusion profiles in mantle olivine. Geology (in press)

Gaetani GA, Grove TL (1998) The influence of water on melting of mantle peridotite. Contrib Mineral Petrol 131:323–346

Hirth G, Evans RL, Chave AD (2000) Comparison of continental and oceanic mantle electrical conductivity: is the Archean lithosphere dry? Geochem Geophys Geosys 1(12), doi:10.1029/2000GC000048

Hudson P, Baker DR, Toft PB (1994) A high-temperature assembly for 1.91 cm (3/4-in) piston-cylinder apparatus. Am Mineral 79:145–147

Ingrin J, Skogby H (2000) Hydrogen in nominally anhydrous upper-mantle minerals: concentration levels and implications. Eur J Minerals 12:543–570

Karato SI (1990) The role of hydrogen diffusivity in the electrical conductivity of the upper mantle. Nature 347:272–273

Karato SI, Paterson MS, Fitz Gerald JD (1986) Rheology of synthetic olivine aggregates: influence of grain size and water. J Geophys Res 91:8151–8176

Kohlstedt DL, Mackwell SJ (1998) Diffusion of hydrogen and intrinsic point defects in olivine. Z Phys Chem 207:147–162

Kohlstedt DL, Mackwell SJ (1999) Solubility and diffusion of "water" in silicate minerals. In: Catlow R (eds) Microscopic properties and processes in minerals. Kluwer, Netherlands, pp 539–559

Kohlstedt DL, Keppler H, Rubie DC (1996) Solubility of water in the $\alpha$, $\beta$ and $\gamma$ phases of $(Mg,Fe)_2SiO_4$. Contrib Mineral Petrol 123:345–357

Lemaire C, Kohn SC, Brooker R (2003) The effect of the silica activity on the incorporation mechanisms of water in synthetic forsterite: a polarized spectroscopic study. Contrib Mineral Petrol 147:48–57

Mackwell SJ, Kohlstedt DL (1990) Diffusion of hydrogen in olivine: implications for water in the mantle. J Geophys Res 95:5079–5088

Mackwell SJ, Kohlstedt DL, Paterson MS (1985) The role of water in the deformation of olivine single crystals. J Geophys Res 90:11,319–11,333

Mackwell SJ, Dimos D, Kohlstedt DL (1988) Transient creep of olivine: point-defect relaxation times. Philo Mag A 57:779–789

Matsyuk SS, Langer K (2004) Hydroxyl in olivines from mantles xenoliths in kimberlites of the Siberian platform. Contrib Mineral Petrol 147:413–437

Matveev S, O'Neill HStC, Ballaus C, Taylor WR, Green DH (2001) Effect of silica activity on $OH^-$ IR spectra of olivine: implications for low-a$SiO_2$ mantle metasomatism. J Petrol 42:721–729

Matveev S, Portnyagin M, Ballhaus C, Brooker R, Geiger CA (2004) FTIR spectrum of phenocryst olivine as an indicator of silica saturation in magmas. J Petrol v. Advance Acces J Petrol, 4th Dec 2004, doi:10.1093/petrology/egh090

Mattioli GS, Wood BJ (1986) Upper mantle oxygen fugacity recorded by spinel lherzolites. Nature 322:626–628

McCammon CA (2005) The paradox of mantle redox. Science 308:807–807

Mei S, Kohlstedt DL (2000) Influence of water on plastic deformation of olivine aggregates 2 dislocation creep regime. J Geophys Res 105:21471–21481

Miller GH, Rossman GR, Harlow GE (1987) The natural occurrence of hydroxide in olivine. Phys Chem Miner 14:461–472

Mosenfelder JL, Deligne NI, Asimow PD, Rossman GR (2006) Hydrogen incorporation in olivine from 2–12 GPa. Am Mineral 91:285–294

Muentener O, Kelemen PB, Grove TL (2001) The role of $H_2O$ during crystallization of primitive arc magmas under uppermost mantle conditions and genesis of igneous pyroxenites:an experimental study. Contrib Mineral Petrol 141:643–658

Nakamura A, Schmalzried H (1983) On the nonstoichiometry and point defects of olivine. Phys Chem Miner 10:27–37

Nakamura A, Schmalzried H (1984) On the $Fe^{2+}$–$Mg^{2+}$ interdiffusion in olivine (II). Ber Bunsen Phys Chem 88:140–145

O'Neill HStC, Wall VJ (1987) The olivine-orthopyroxene-spinel oxygen geobarometer, the nickel precipitation curve, and the oxygen fugacity of Earth's upper mantle. J Petrol 28:1169–1191

Paterson MS (1982) The determination of hydroxyl by infrared absorption in quartz, silicate glasses and similar materials. Bull Minéral 105:20–29

Raterron P, Chopra P, Doukhan JC (2000) $SiO_2$ precipitation in olivine: ATEM investigation of two dunites annealed at 300 MPa in hydrous conditions. Earth Planet Sci Lett 180:415–423

Regenauer-Lieb K, Kohl T (2003) Water solubility and diffusivity in olivine: its role in planetary tectonics. Mineral Mag 67(4):697–715

Regenauer-Lieb K, Yuen D, Branlund J (2001) The initiation of subduction: criticaly by addition of water? Science 294:578–580

Sato H (1986) High temperature ac electrical properties of olivine single crystal with varying oxygen partial pressure: implications for the point defect chemistry. Earth Planet Inter 41:269–282

Tsai TL, Dieckmann R (1997) Point defect and transport of matter and charge in olivines $(Fe_xMg_{1-x})_2SiO_4$. Mat Sci Forum 239–241:399–402

Tsai TL, Dieckmann R (2002) Variation of the oxygen content and point-defects in olivines $(Fe_xMg_{1-x})_2SiO_4$, $0.2 < x < 1.0$. Phys Chem Miner 29:680–694

Wanamaker BJ (1994) Point defect diffusivities in San Carlos olivine derived from reequilibration of electrical conductivity following changes in oxygen fugacity. Geophys Res Lett 21:21–24

Zhao YH, Ginsberg SB, Kohlstedt DL (2004) Solubility of hydrogen in olivine: dependence on temperature and iron content. Contrib Mineral Petrol 147:155–161